

Supporting Information

FePb-doped RuO₂ coupled amorphous/crystalline heterophase for efficient acidic

oxygen evolution reaction

Yan Zhao,[#] Yu Long,[#] Wenwen Liu, Zhenyong Han, Yuteng Cui, Zhijun Li, Wanglei

Wang, Zhiyao Duan,* Xiaogang Fu*

State Key Laboratory of Solidification Processing, Atomic Control & Catalysis

Engineering Laboratory, School of Materials Science and Engineering, Northwestern

Polytechnical University, Xi'an, Shaanxi, 710072, P. R. China

Experimental section

Materials

All reagents were used as received without further purification. Ruthenium (III) acetylacetonate ($\text{Ru}(\text{acac})_3$, 97%, Aladdin), iron acetylacetonate ($\text{Fe}(\text{acac})_3$, 98%, TCI), acetylacetonate lead ($\text{Pb}(\text{acac})_2$, 99%, Alfa Aesar) were used as precursors. Hexadecylamine (HDA, 95%, TCI) was used as a ligand. N, N-Dimethylformamide (DMF, AR, Sinopharm Chemical Reagent Co., Ltd) was used as the solvent. Ruthenium oxide (RuO_2 , 99.9%, Aldrich) was used as a standard for comparison. Hexane and ethanol are reagent grade. Ti fiber (Sti040-Pt0.5) was purchased from Suzhou Siner Technology Co., Ltd, Ti fiber with a thickness of 40 μm and Pt loading of 0.5 $\text{mg}\cdot\text{cm}^{-2}$.

Characterization

Transmission electron microscope (TEM), high-resolution transmission electron microscope (HRTEM), high-angle annular dark-field scanning TEM (HAADF-STEM) and Energy-dispersive Spectroscopic (EDS) element mapping images were characterized using a Talos F200x transmission electron microscope at 200 kV. The X-ray diffraction (XRD) patterns were obtained by using the Ultima IV with $\text{Cu K}\alpha$ radiation. The X-ray Photoelectron Spectroscopy (XPS) data were obtained using X-ray Scientific K-Alpha + analysis of photoelectron spectroscopy.

Electrochemical Measurements

All electrochemical measurements were carried out in a three-electrode system on an electrochemical workstation (Autolab 204/302). The electrochemical performance was tested

in 0.5 M H₂SO₄ purged with pure Ar and using a platinum wire as the counter electrode, Ag/AgCl (in saturated KCl solution) electrode as the reference electrode, and the catalyst-loaded Ti fiber as the working electrode. The test methods included cyclic voltammetry (CV), linear sweep voltammetry (LSV), chronopotentiometry (CP), electrochemical impedance spectrum (EIS), and double-layer capacitance (C_{dl}). To ensure the accuracy of the experiment, the Ag/AgCl reference electrode was required to be calibrated before electrochemical measurements. All potentials measured were converted to the reversible hydrogen electrode (RHE) scale using: $E_{\text{RHE}} = E_{\text{Ag/AgCl}} + 0.223 - 0.236 \text{ V}$. LSV tests were conducted with a scan rate of 10 mV·s⁻¹. Stability was tested by chronopotentiometry at 10 mA·cm⁻². EIS tests were performed at 1.45 V (versus RHE) from 0.1 Hz to 100 kHz, and the results were presented in the form of a Nyquist plot. C_{dl} was calculated by the equation $C_{\text{dl}} = i_c / \nu$, where i_c was the charging current and ν was the scan rate. A series of CV tests were performed in the non-faradaic potential region 1.1–1.2 V (versus RHE) under different scan rates (10, 15, 20 and 25 mV·s⁻¹). Then by plotting measured i_c versus ν , C_{dl} was obtained from the slopes of the linear fitting. Electrochemical active surface area (ECSA) can be calculated by the equation $\text{ECSA} = C_{\text{dl}} / C_s$, where C_s is the specific capacitance, and the typical value is 0.035 mF·cm⁻².

PEMWE tests

The self-made cell was employed as the PEMWE device and Nafion 115 was selected for the proton exchange membrane. About 0.2 mg·cm⁻² commercial Pt/C was used as the HER cathode, and Ti fiber as the cathode gas diffusion layer. About 3 mg·cm⁻² FePb-RuO₂ catalyst with 1 wt.% polytetrafluoroethylene binder was drop-cast onto the Ti fiber electrode. After

drying, the electrode was pressed at 150 °C under the pressure of 10 MPa by a regular hot-press machine, which was used as an OER anode and circulated with 0.5 M H₂SO₄ solution. I-V curves were measured at 0–1200 mA·cm⁻² at 60 °C. The stability test was performed at 100 mA·cm⁻². All cell voltages measured in this PEMWE electrolyzers were without iR compensation.

Computational details

The Density Functional Theory (DFT) was conducted using the Vienna ab initio Simulation Package (VASP) codes.¹⁻³ The projector augmented wave (PAW)⁴ method was used to describe the core electrons. The generalized gradient approximation (GGA) with Perdew-Burke-Ernzerhof (PBE)⁵ was used for the exchange-correlation function. In all calculations, the plane waves had a cut-off energy of 400 eV, and the k-point meshes for the Brillouin zone were obtained using the special-point sampling technique of Monkhorst and Pack, with (2 × 2 × 1) sampling meshes for the slab.⁶ Convergence criteria of 10⁻⁵ eV were applied to the electronic relaxations. Ispin was set to 2, and spin was turned on. A Debye length of 3 Å was set to mimic the experimental condition with a strong acid solution (pH = 0). Atomistic Simulation Environment (ASE) package software calculation methods were applied to the establishment of our model.

In this study, RuO₂ with a rutile structure was modeled. The optimized lattice constants for the rutile RuO₂ were calculated to be a = b = 4.543 Å, c/a = 0.691 Å, which was consistent with a theoretical value of a = 4.48 Å and c/a = 0.694.⁷ A (4 × 2) unit cell with 4 layers of RuO₂ (110) surfaces was modeled. The bottom layer of the slab was fixed in position to mimic a bulk

RuO₂ while all other atoms were relaxed into their stable states by a conjugate-gradient algorithm. A 15 Å vacuum gap was introduced in all the slab models to eliminate the interaction between periodic images along the z direction. Based on this established model, we doped metal elements such as Fe or Pb.

For the computation of the electrochemical free energy, the change of each elementary step could be expressed as $\Delta G = \Delta E - T\Delta S + \Delta ZPE$, where T, ΔE , ΔS , ΔZPE denoted the temperature, total energy change of the elementary steps, the entropic change, and the change of zero-point energy. In our study, the entropic contribution of the adsorbed species was ignored. The zero-point energy contributions to the reaction free energy were not taken into account since they were normally negligible as compared to ΔE and $T\Delta S$. The chemical potential of the solvated proton and electron pair ($H^+ + e^-$) at standard conditions (pH=0, T=298.15 K) was calculated as $1/2G_{H_2} + eU_{SHE}$, assuming equilibrium at the standard hydrogen electrode (SHE) according to the computational electrode method.⁸ The $T\Delta S$ of aqueous H₂O was

0.67 eV.⁸

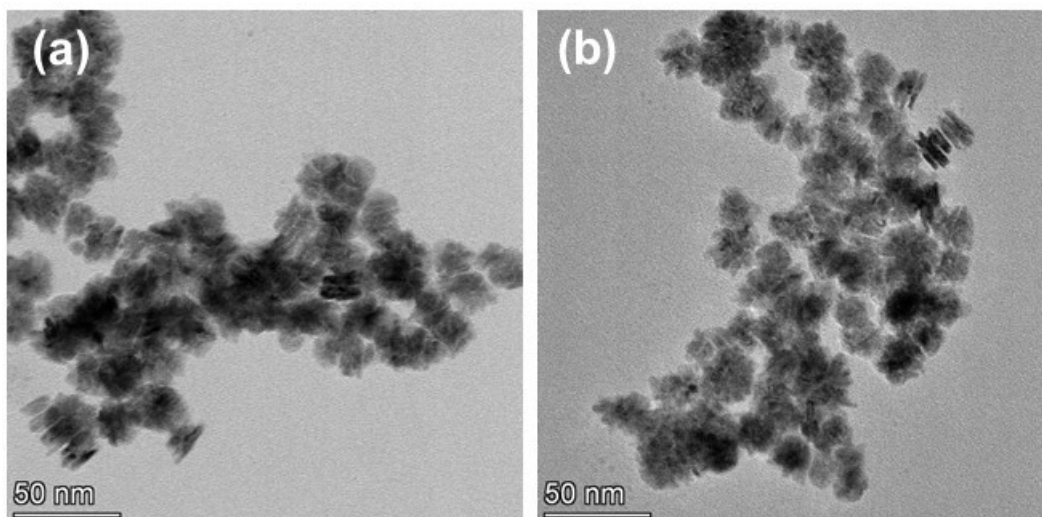


Fig. S1. (a, b) TEM images of FePb-Ru.

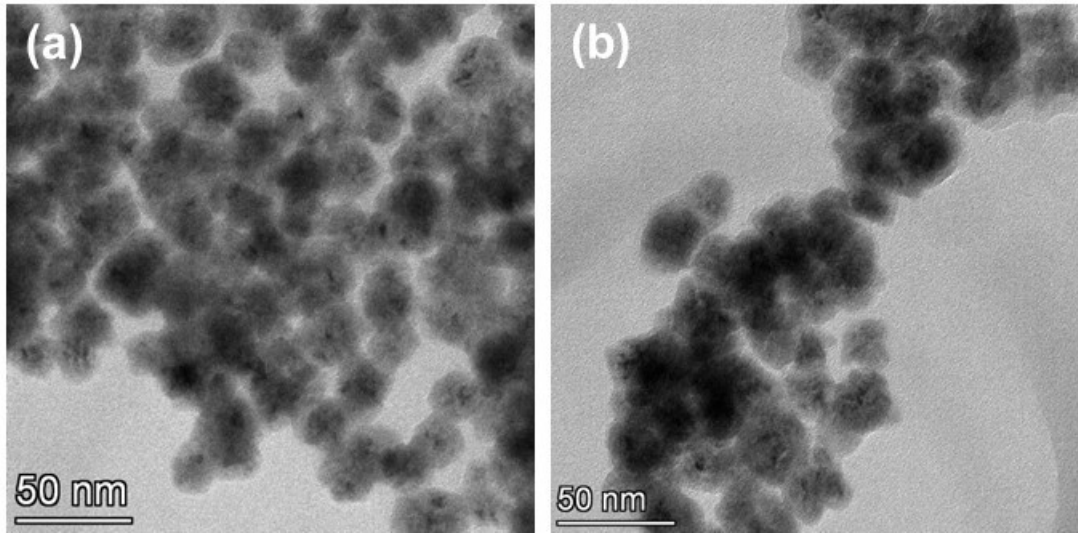


Fig. S2. (a, b) TEM images of FePb-RuO₂.

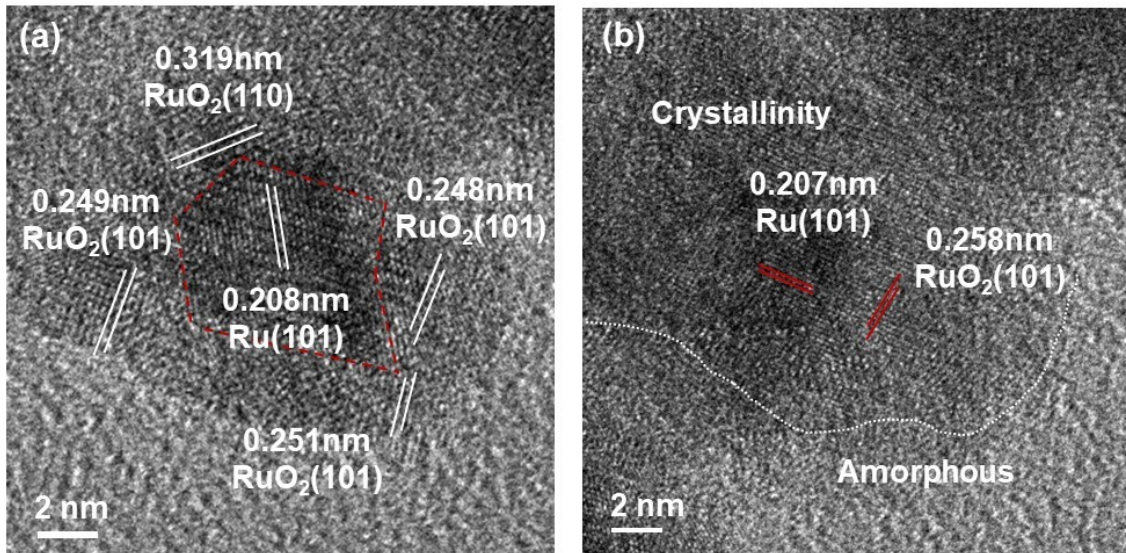


Fig. S3. HRTEM images of FePb-RuO₂.

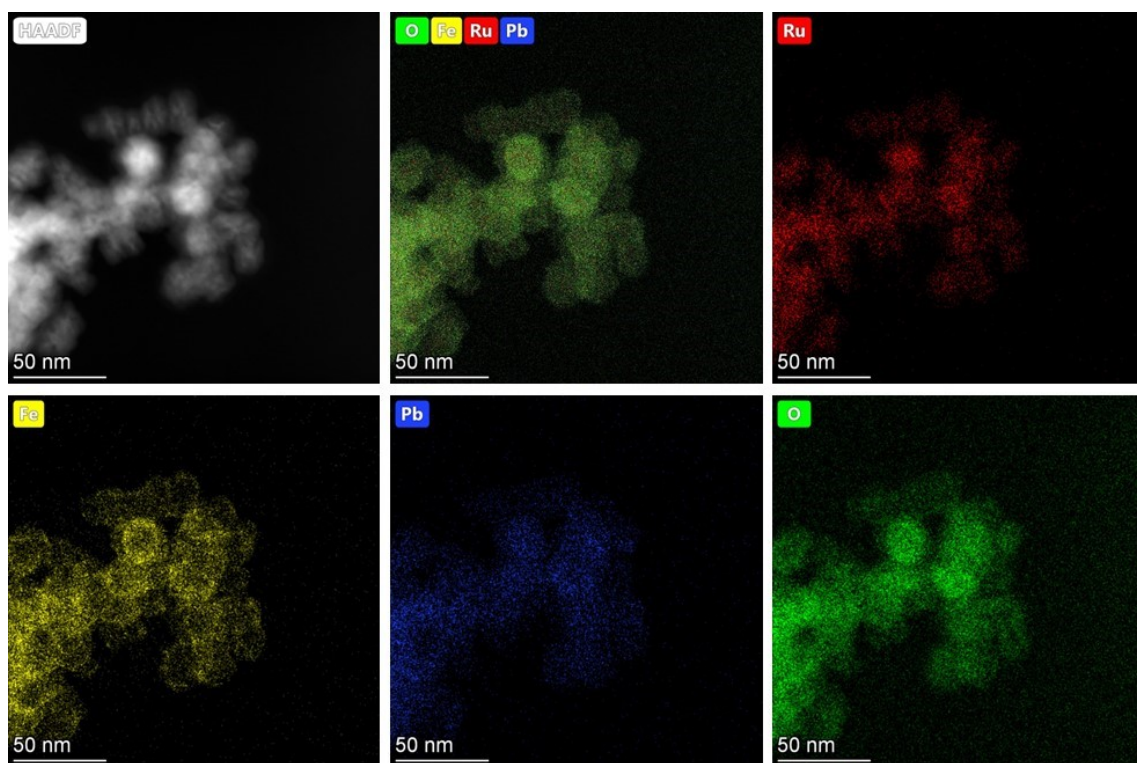


Fig. S4. HADDF-STEM and EDS mapping images of FePb-RuO₂.

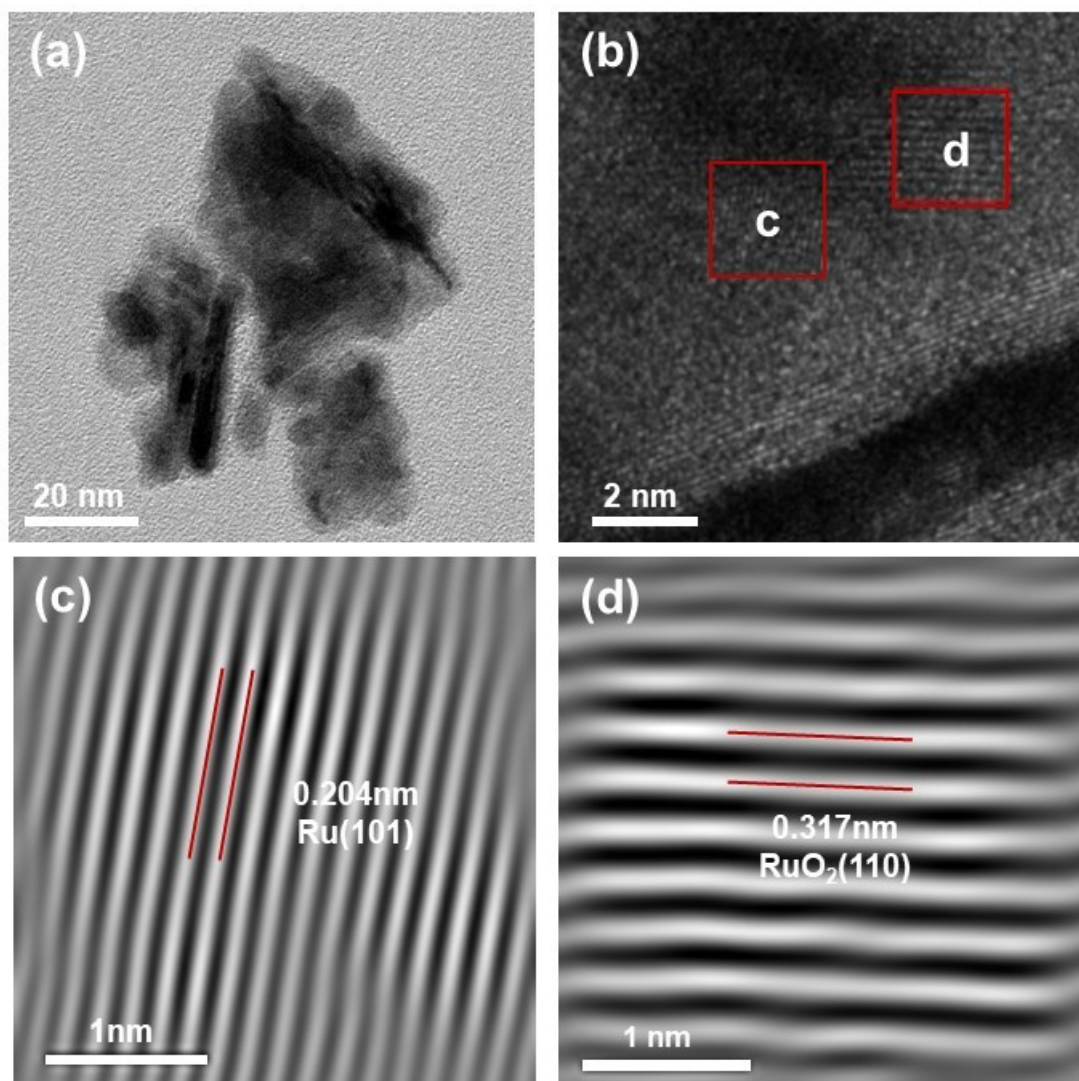


Fig. S5. (a) TEM image, (b) HRTEM image and (c, d) inverse FFT images of Hm-RuO₂.

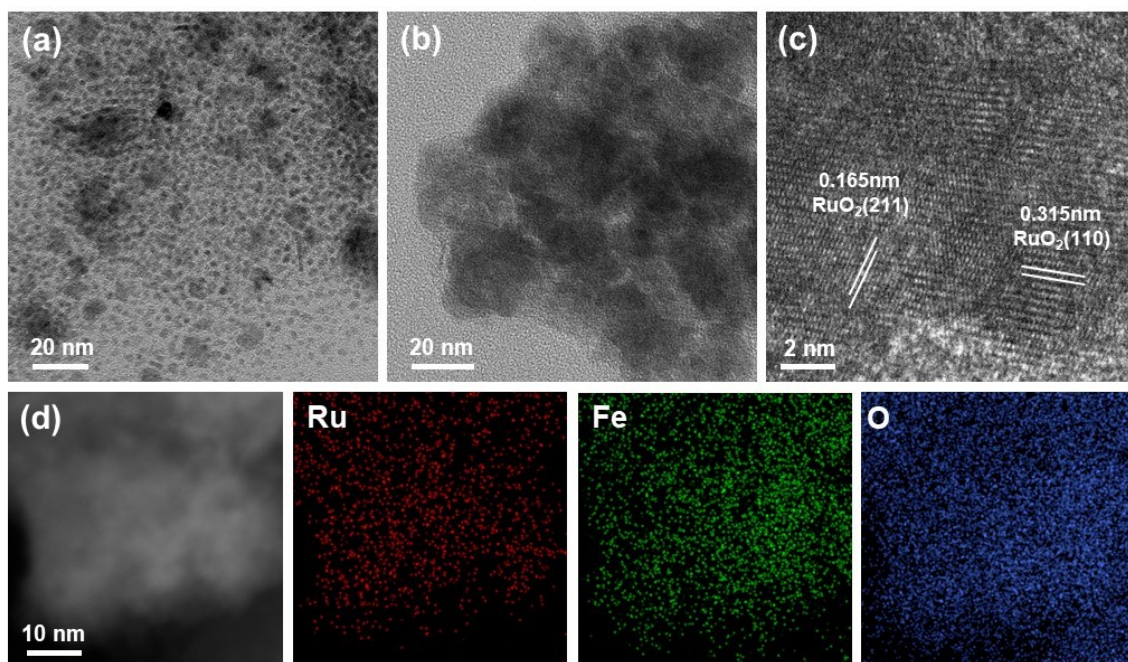


Fig. S6. (a) TEM image of Fe_1Ru_9 , (b) TEM image of Fe-RuO_2 , (c) HRTEM image of Fe-RuO_2 , (d) HAADF-STEM and EDS mapping images of Fe-RuO_2 .

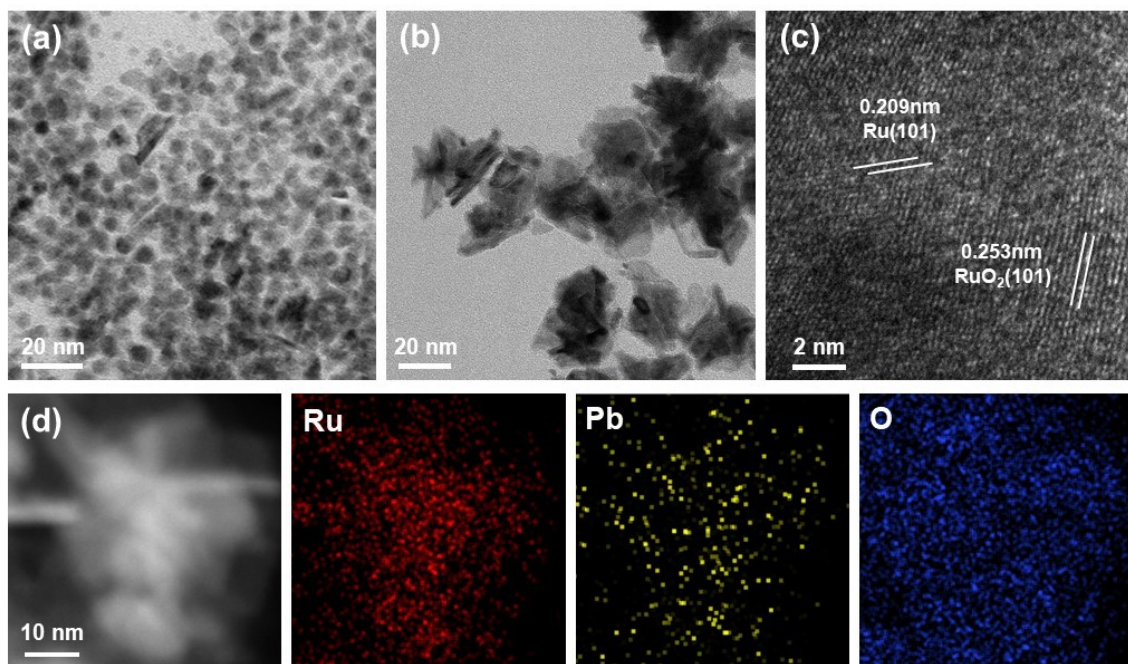


Fig. S7. (a) TEM image of Pb_1Ru_9 , (b) TEM image of $Pb-RuO_2$, (c) HRTEM image of $Pb-RuO_2$, (d) HAADF-STEM and EDS mapping images of $Pb-RuO_2$.

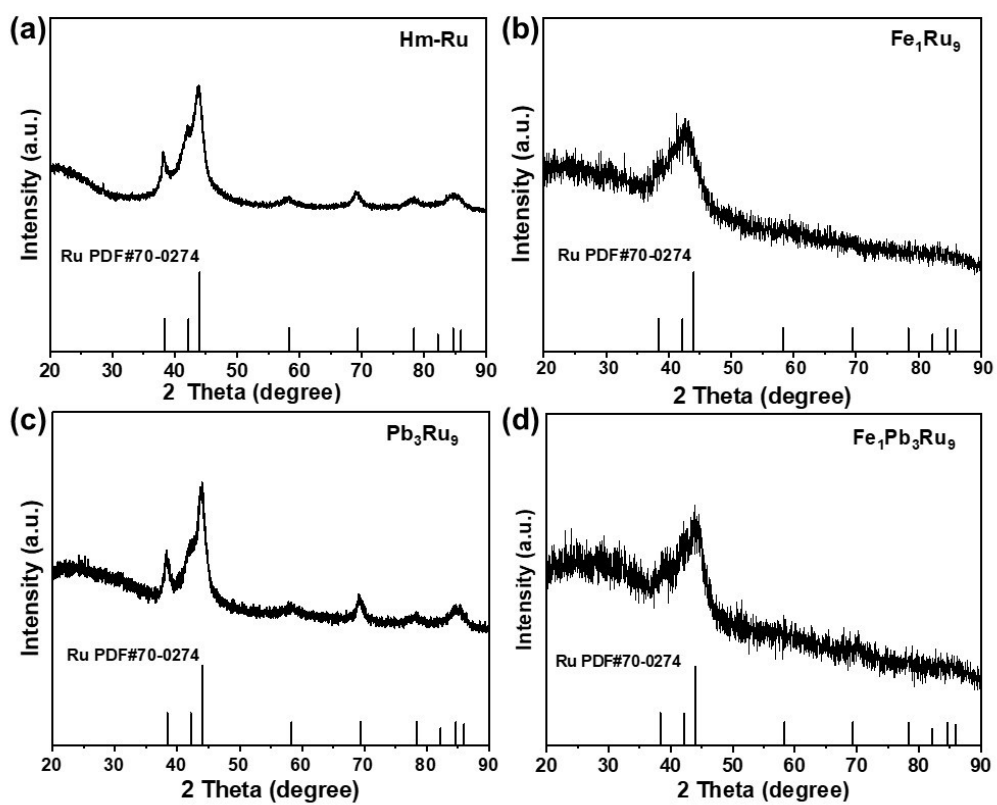


Fig. S8. XRD patterns of (a) Hm-Ru, (b) Fe₁Ru₉, (c) Pb₃Ru₁ and (d) Fe₁Pb₃Ru₉ catalysts.

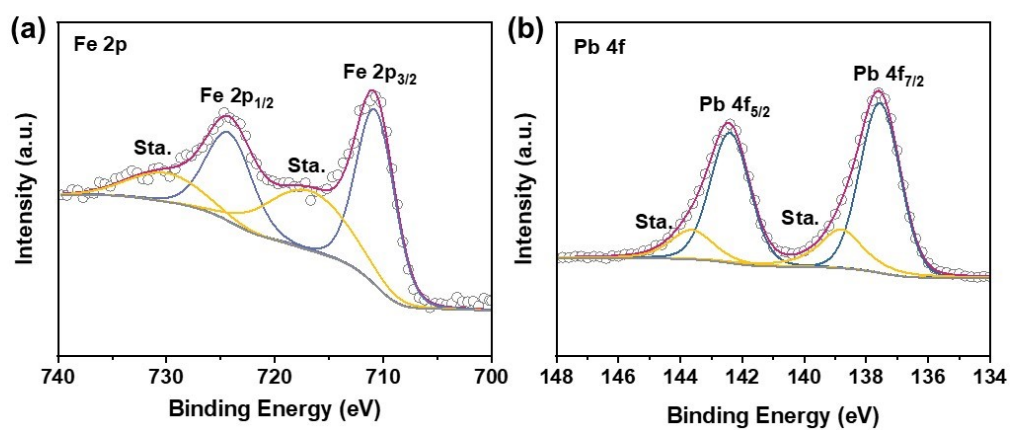


Fig. S9. (a) Fe 2p XPS spectra of FePb-RuO₂, (b) Pb 4f XPS spectra of FePb-RuO₂.

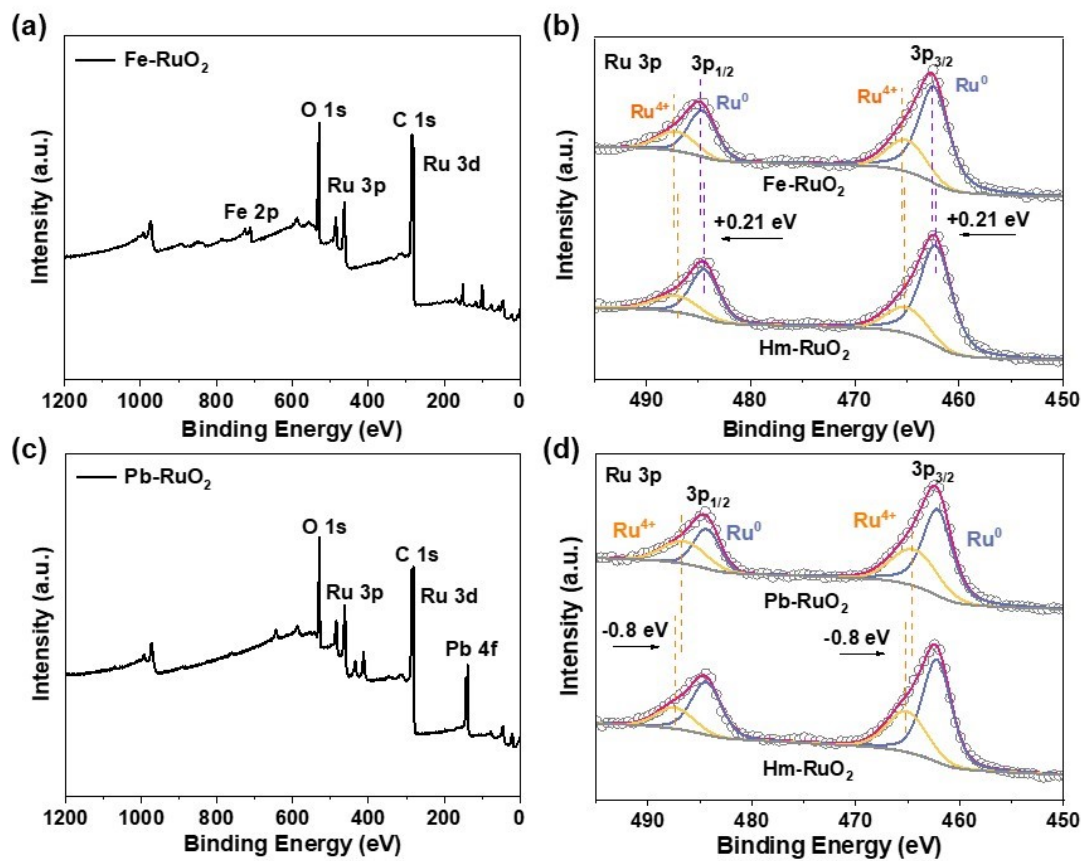


Fig. S10. XPS spectra of (a, b) Fe-RuO₂ and (c, d) Pb-RuO₂.

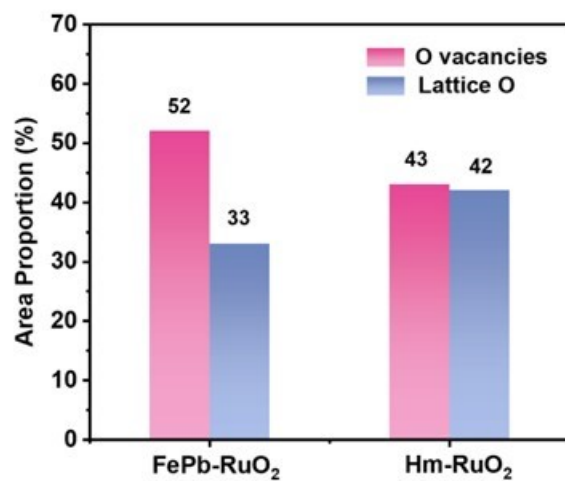


Fig. S11. The area proportion of O vacancies and lattice O in FePb-RuO₂ and RuO₂.

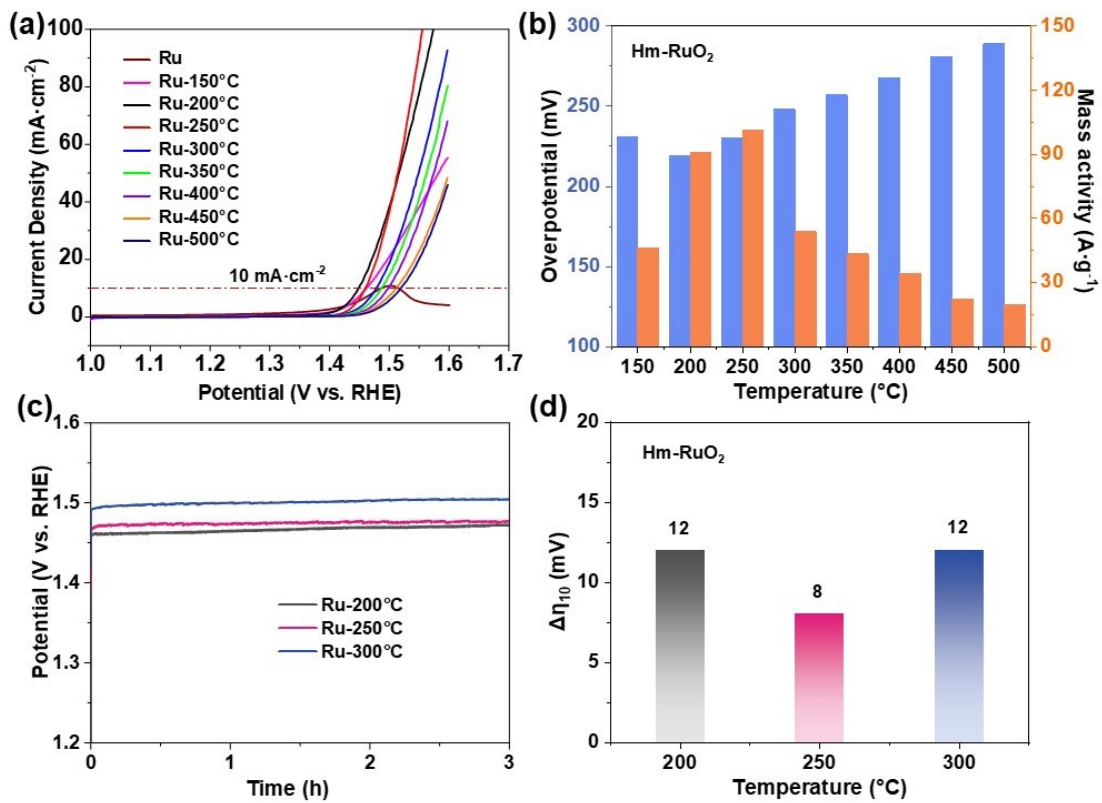


Fig. S12. OER performance test of Hm-RuO₂ catalysts oxidized at different temperatures in 0.5 M H₂SO₄ solution: (a) LSV curves, (b) OER overpotential at $10\text{ mA}\cdot\text{cm}^{-2}$, (c) chronopotentiometry testing at $10\text{ mA}\cdot\text{cm}^{-2}$, (d) the increased overpotential ($\Delta\eta$) after chronopotentiometry testing.

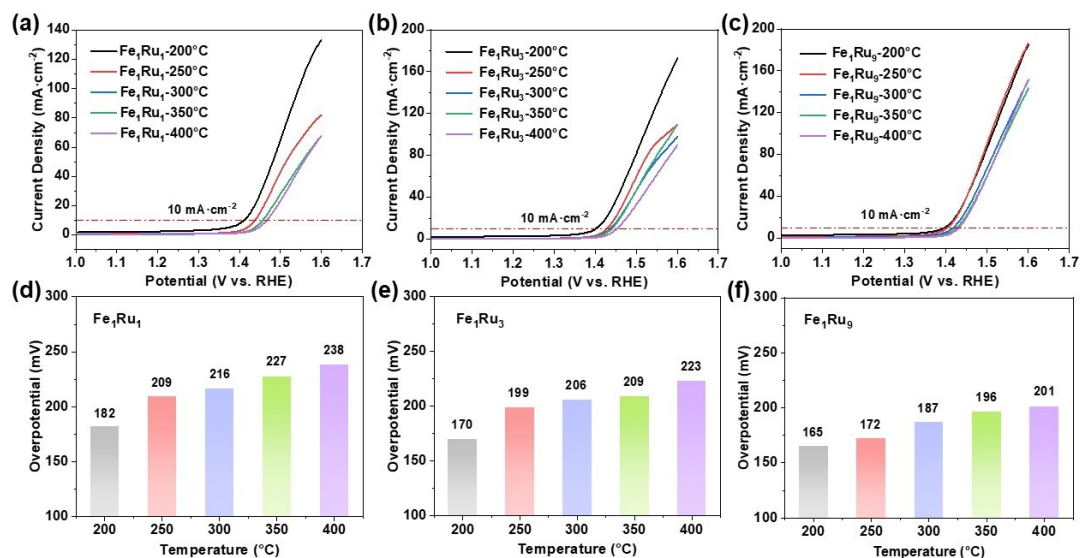


Fig. S13. OER performance test of Fe-RuO₂ catalysts oxidized at different temperatures in 0.5 M H₂SO₄ solution: LSV curves of (a) Fe₁Ru₁, (b) Fe₁Ru₃, (c) Fe₁Ru₉; OER overpotential at 10 mA·cm⁻² of (d) Fe₁Ru₁, (e) Fe₁Ru₃, (f) Fe₁Ru₉.

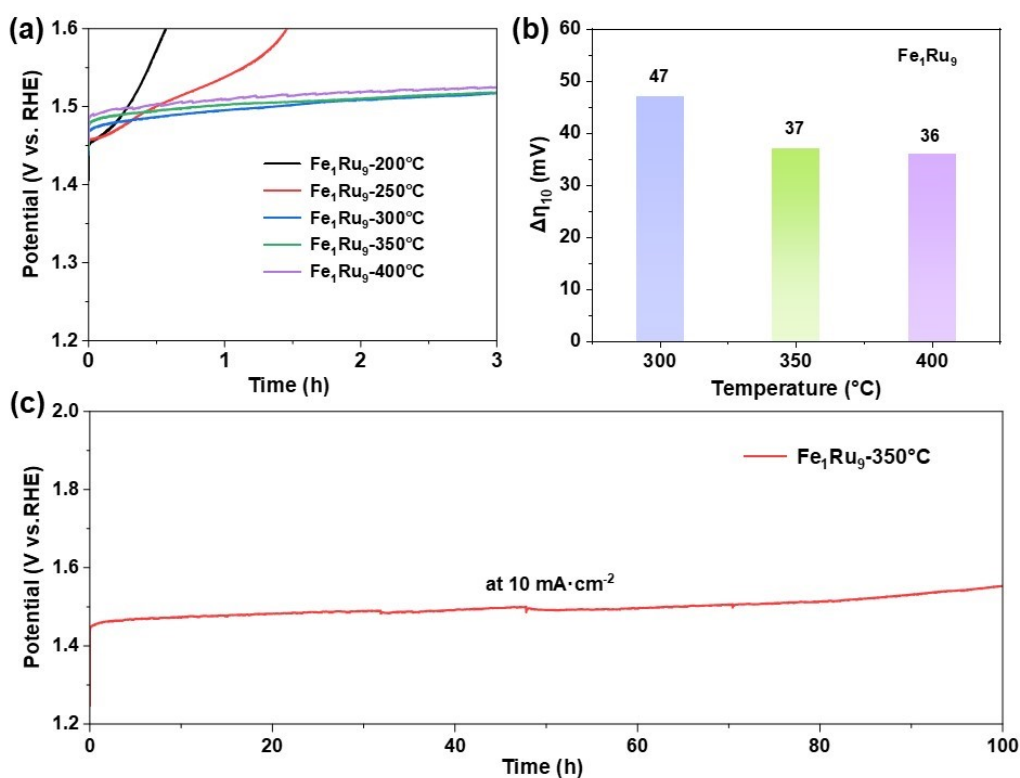


Fig. S14. OER performance test of Fe₁Ru₉ catalysts oxidized at different temperatures in 0.5 M H₂SO₄ solution: (a) chronopotentiometry testing at 10 mA·cm⁻² for 3 h, (b) the increased overpotential ($\Delta\eta$) after chronopotentiometry testing 3 h, (c) chronopotentiometry testing at 10 mA·cm⁻² for 100 h of Fe₁Ru₉-350 °C.

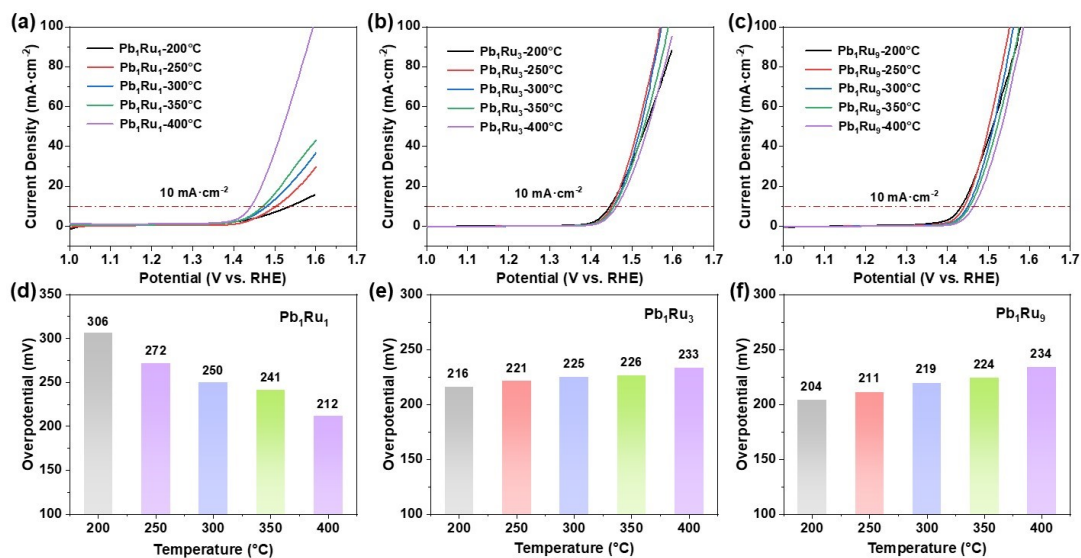


Fig. S15. OER performance test of Pb-RuO₂ catalysts oxidized at different temperatures in 0.5 M H₂SO₄ solution: LSV curves of (a) Pb₁Ru₁, (b) Pb₁Ru₃, (c) Pb₁Ru₉; OER overpotential at 10 mA·cm⁻² of (d) Pb₁Ru₁, (e) Pb₁Ru₃, (f) Pb₁Ru₉.

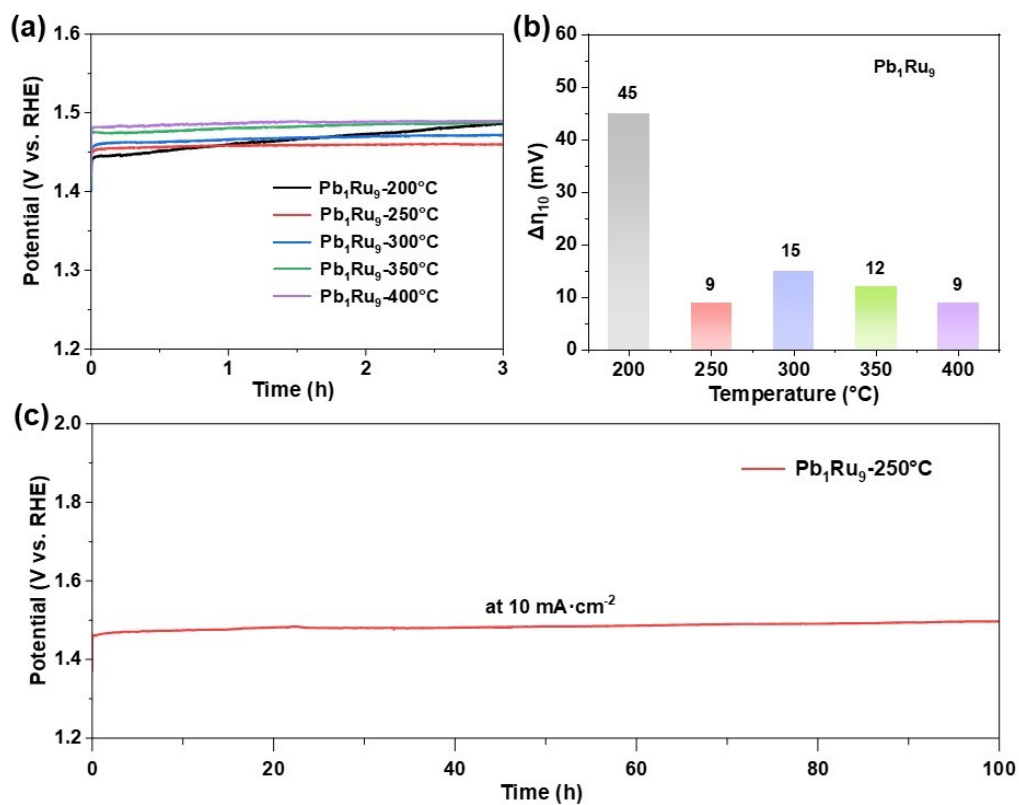


Fig. S16. OER performance test of Pb_1Ru_9 catalysts oxidized at different temperatures in $0.5 \text{ M H}_2\text{SO}_4$ solution: (a) chronopotentiometry testing at $10 \text{ mA}\cdot\text{cm}^{-2}$ for 3 h, (b) the increased overpotential ($\Delta\eta$) after chronopotentiometry testing 3 h, (c) chronopotentiometry testing at $10 \text{ mA}\cdot\text{cm}^{-2}$ for 100 h of Pb_1Ru_9 - 250°C .

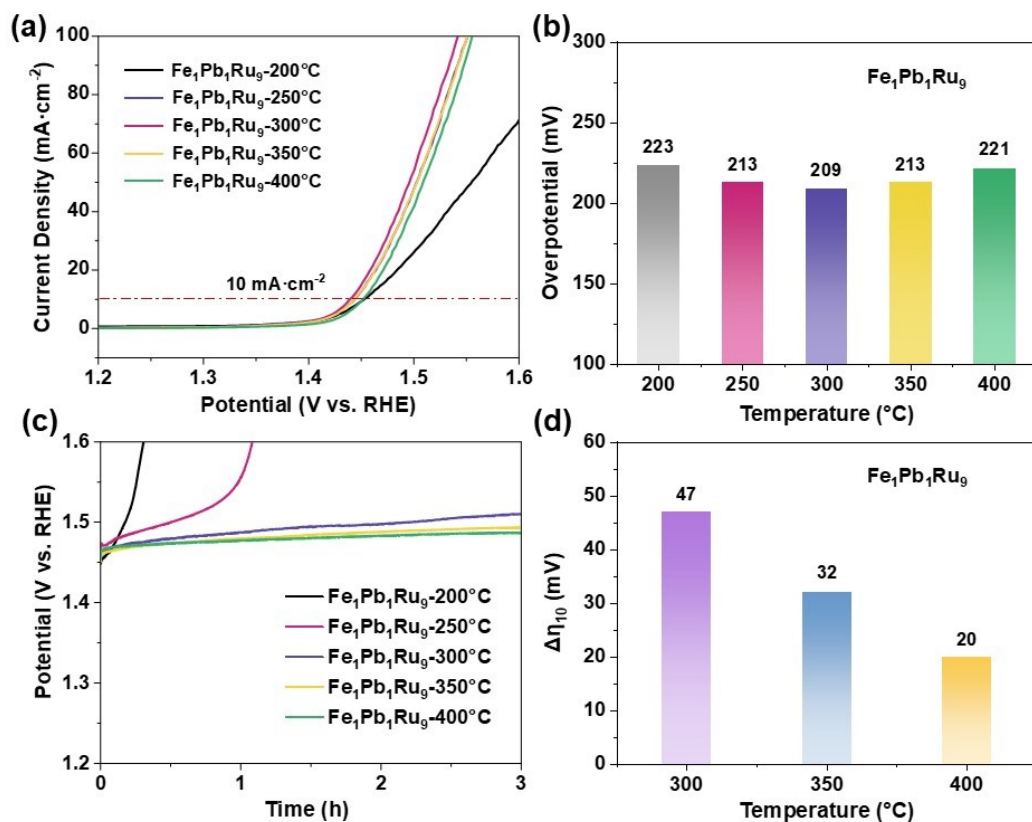


Fig. S17. OER performance test of $\text{Fe}_1\text{Pb}_1\text{Ru}_9$ catalysts synthesized at different temperatures in 0.5 M H_2SO_4 solution: (a) LSV curves, (b) OER overpotential at $10 \text{ mA}\cdot\text{cm}^{-2}$, (c) chronopotentiometry testing at $10 \text{ mA}\cdot\text{cm}^{-2}$, (d) the increased overpotential ($\Delta\eta$) after chronopotentiometry testing.

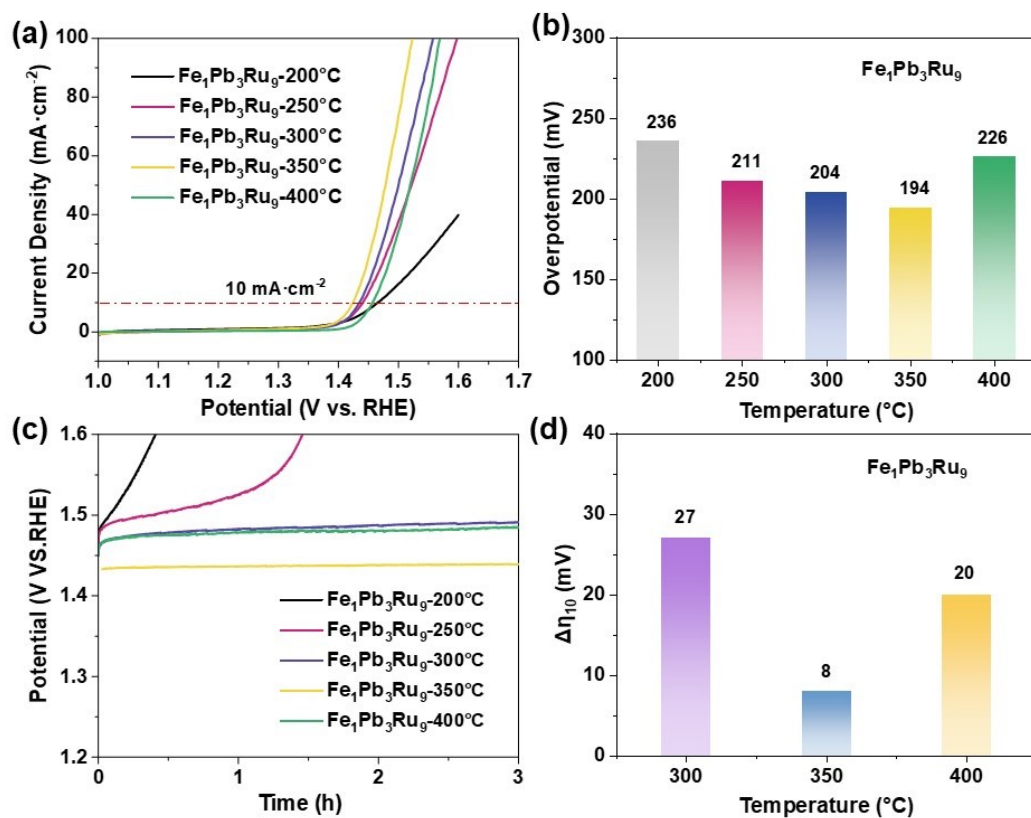


Fig. S18. OER performance test of $\text{Fe}_1\text{Pb}_3\text{Ru}_9$ catalysts synthesized at different temperatures in 0.5 M H_2SO_4 solution: (a) LSV curves, (b) OER overpotential at $10 \text{ mA}\cdot\text{cm}^{-2}$, (c) chronopotentiometry testing at $10 \text{ mA}\cdot\text{cm}^{-2}$, (d) the increased overpotential ($\Delta\eta$) after chronopotentiometry testing.

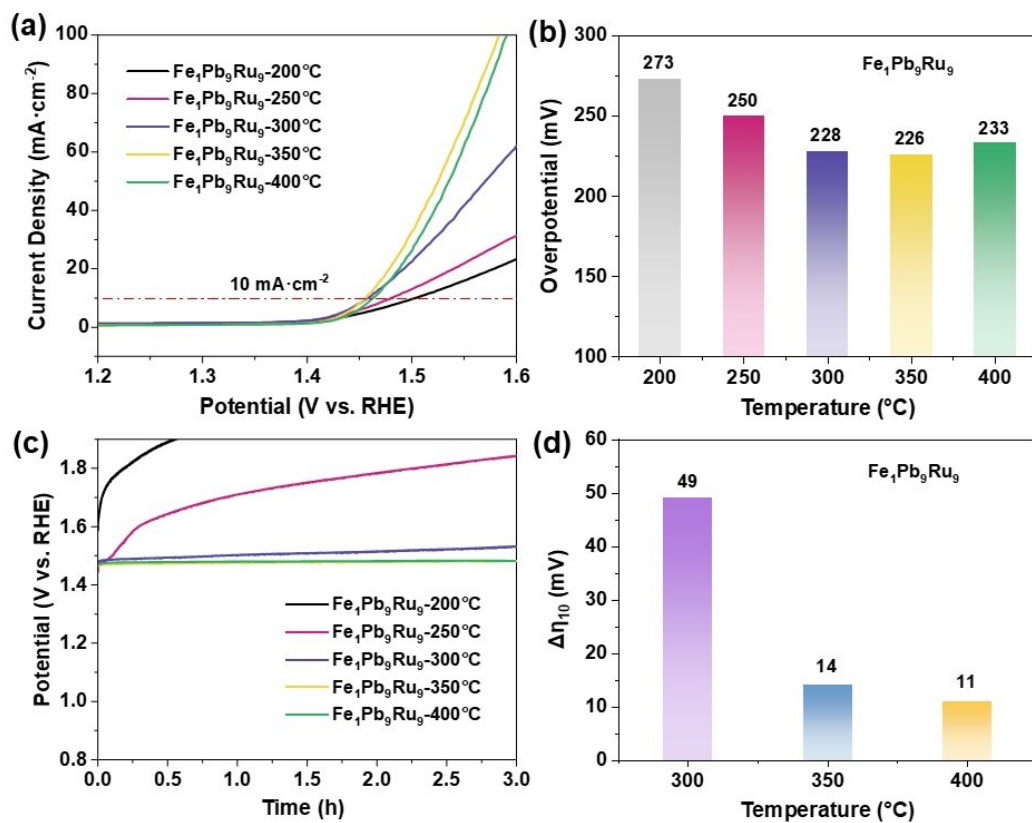


Fig. S19. OER performance test of $\text{Fe}_1\text{Pb}_9\text{Ru}_9$ catalysts synthesized at different temperatures in 0.5 M H_2SO_4 solution: (a) LSV curves, (b) OER overpotential at $10\text{ mA}\cdot\text{cm}^{-2}$, (c) chronopotentiometry testing at $10\text{ mA}\cdot\text{cm}^{-2}$, (d) the increased overpotential ($\Delta\eta$) after chronopotentiometry testing.

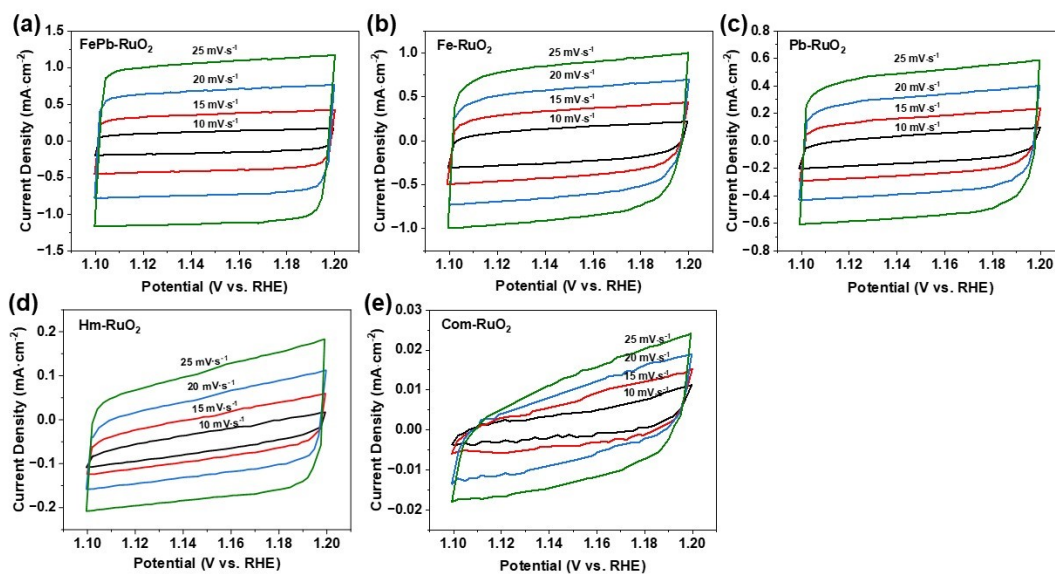


Fig. S20. CV curves of (a) FePb-RuO₂, (b) Fe-RuO₂, (c) Pb-RuO₂, (d) Hm-RuO₂, (e) Com-RuO₂ catalysts at different scan rates from 10 to 25 mV·s⁻¹, respectively.

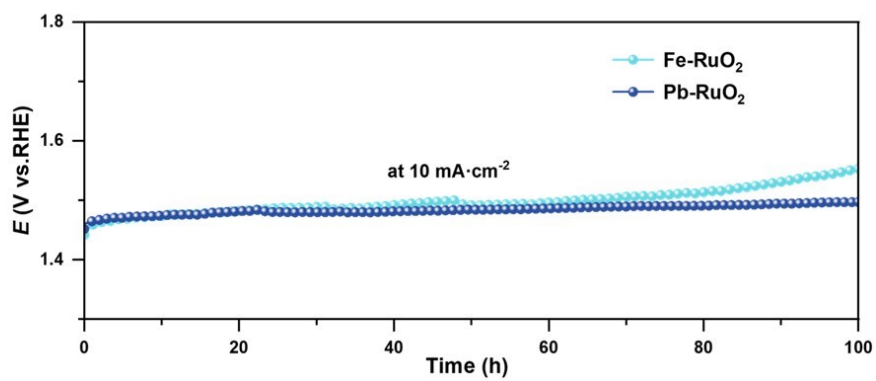


Fig. S21. Chronopotentiometry testing of FePb-RuO₂, Fe-RuO₂, Pb-RuO₂, Hm-RuO₂, and Com-RuO₂ catalysts at 10 mA·cm⁻².

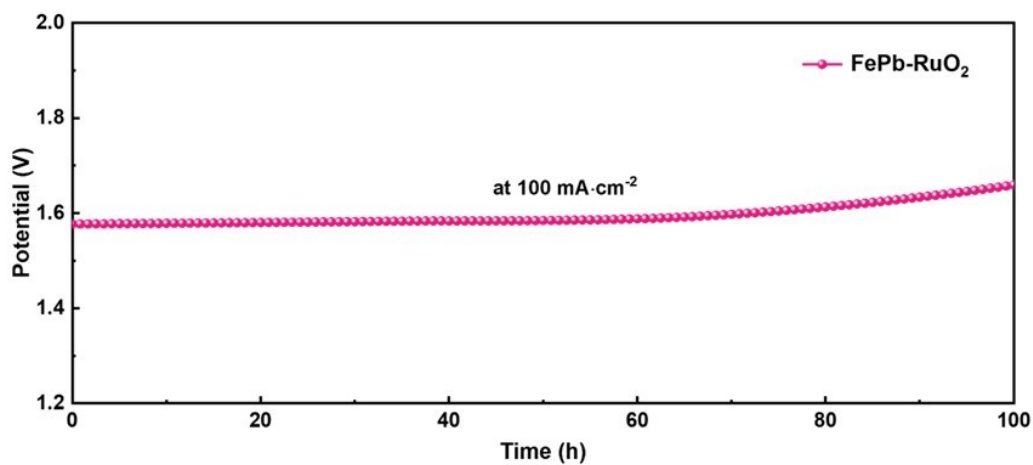


Fig. S22. Chronopotentiometry test of FePb-RuO₂ at current density of 100 mA·cm⁻².

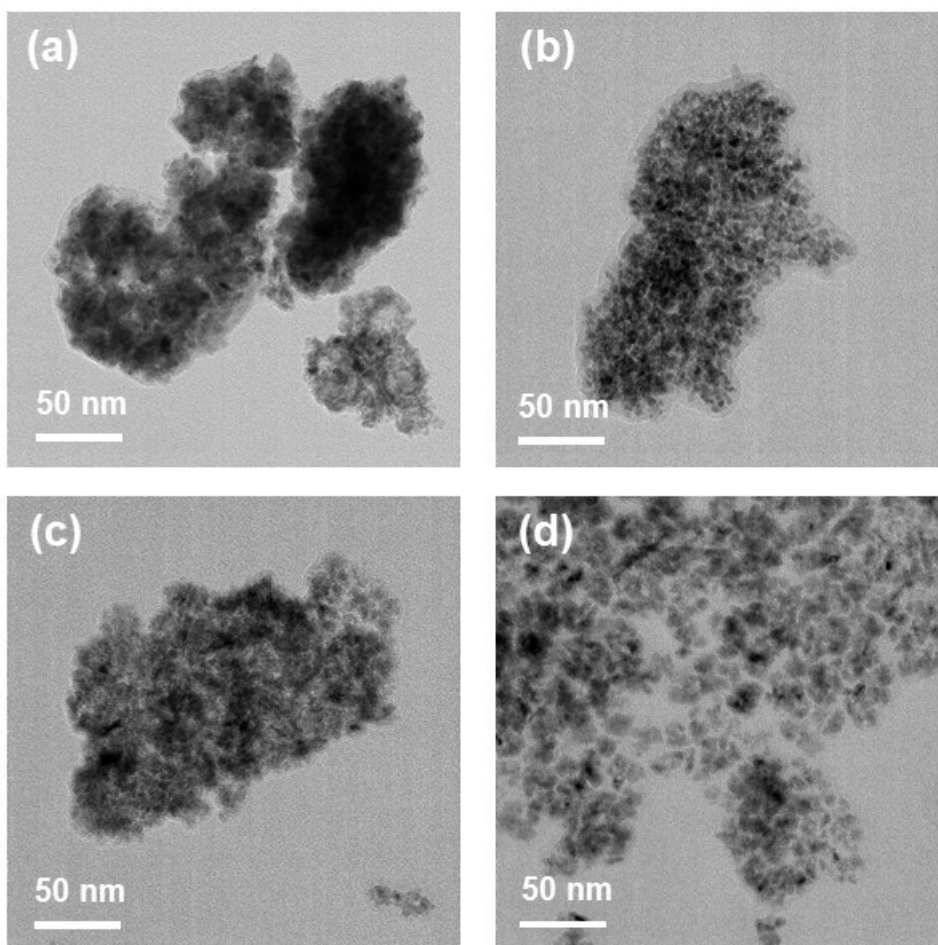


Fig. S23. TEM images of (a) Hm-RuO₂, (b) Fe-RuO₂, (c) Pb-RuO₂ and (d) FePb-RuO₂ after OER.

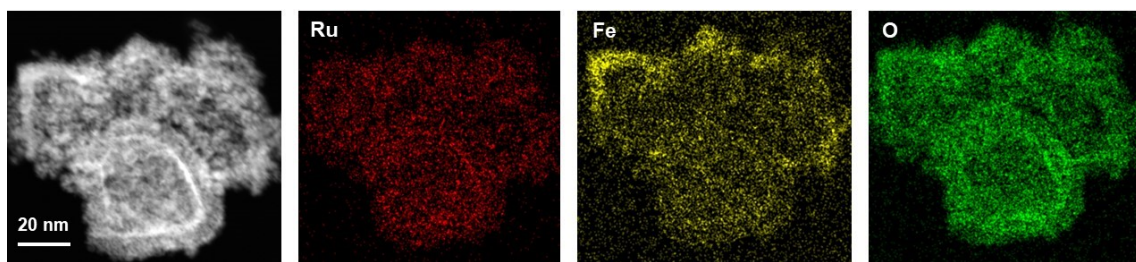


Fig. S24. HADDF-STEM and EDS mapping images of Fe-RuO₂ after OER.

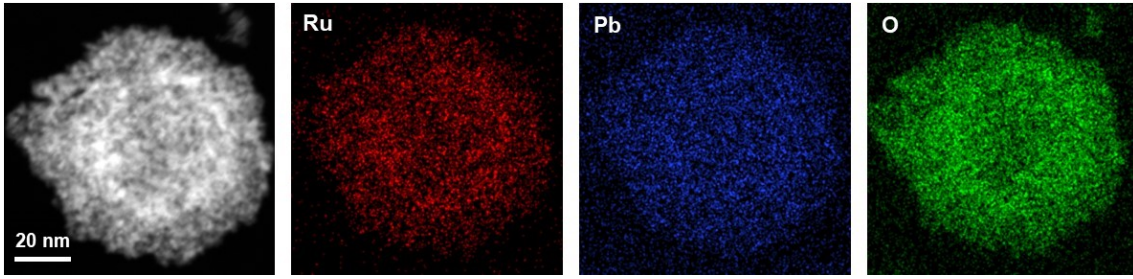


Fig. S25. HADF-STEM and EDS mapping images of Pb-RuO₂ after OER.

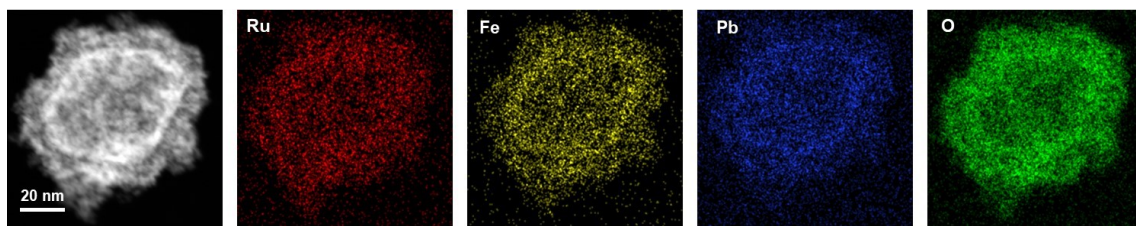


Fig. S26. HADF-STEM and EDS mapping images of FePb-RuO₂ after OER.

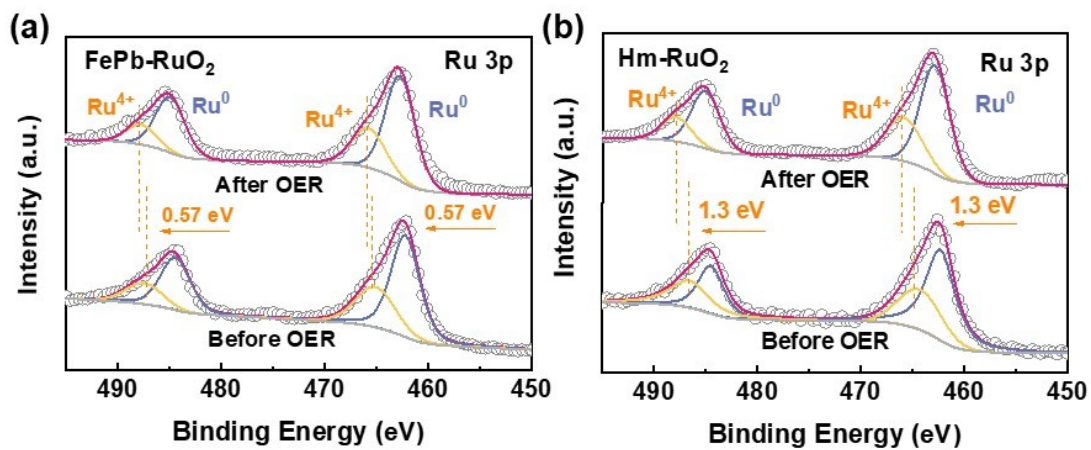


Fig. S27. XPS spectra of Ru 3p in (a) FePb-RuO₂ and (b) Hm-RuO₂ after OER.

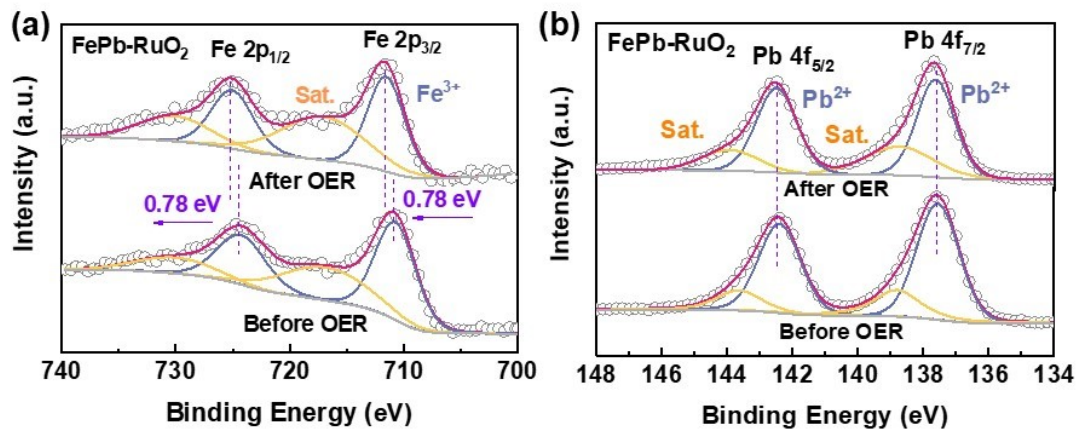


Fig. S28. XPS spectra of (a) Fe 2p and (b) Pb 4f in FePb-RuO₂ after OER.

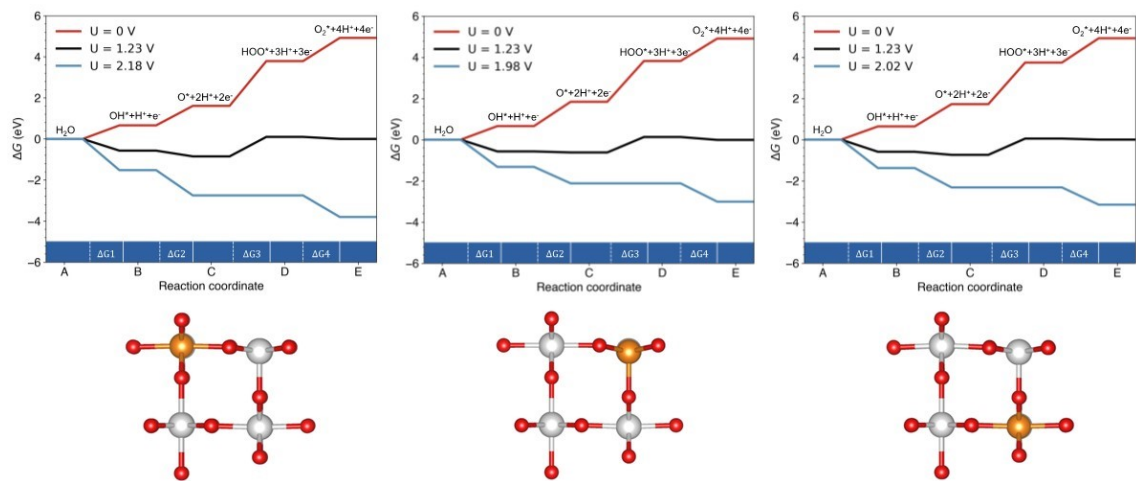


Fig. S29. The free energy diagram of Fe-RuO_2 at site1, site2 and site3.

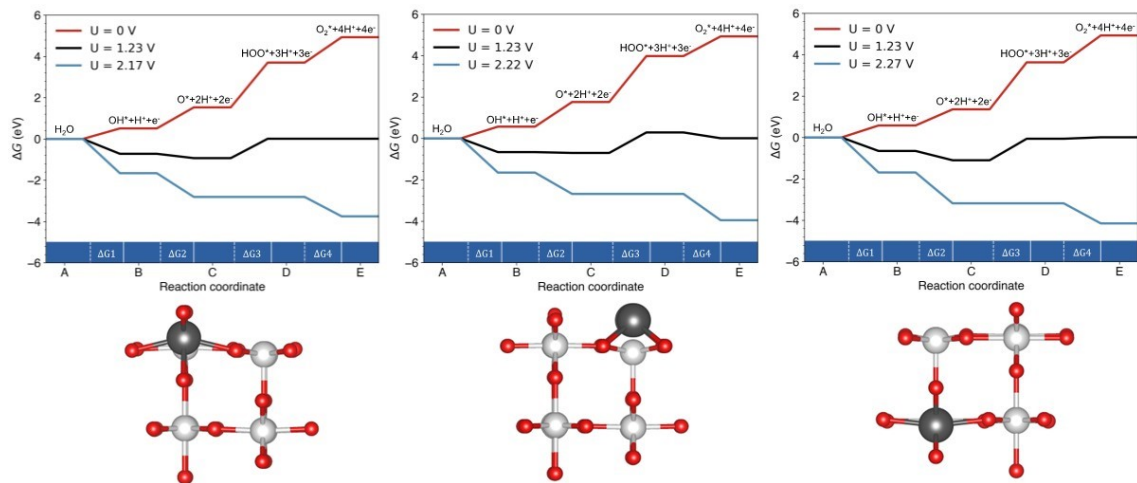


Fig. S30. The free energy diagram of Pb-RuO₂ at site1, site2 and site3.

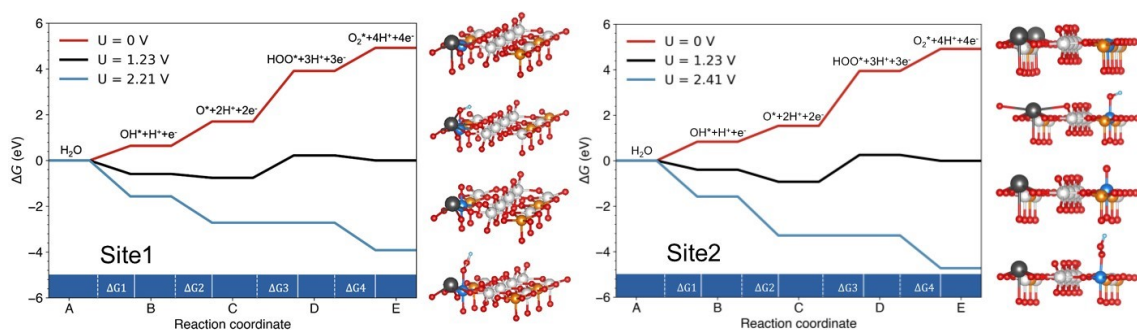


Fig. S31. The free energy diagram of FePb-RuO₂ at site1 and site2.

Table S1. ICP-OES results for the catalyst before OER.

Catalyst	Ru (mg)	Other elements (mg)	Atomic ratio
FePb-RuO ₂	0.985	Fe-0.069 Pb-0.663	Ru:Fe:Pb=9:1:3
Fe-RuO ₂	0.986	Fe-0.071	Ru:Fe=9:1
Pb-RuO ₂	0.979	Pb-0.707	Ru:Fe=3:1

Table S2. The impedance fitting data of different catalysts.

Catalyst	R_s (Ω)	R_f (Ω)	R_{ct} (Ω)
FePb-RuO ₂	1.51	1.08	5.58
Fe-RuO ₂	1.24	1.63	11.2
Pb-RuO ₂	1.20	1.72	13.4
Hm-RuO ₂	1.79	1.23	14.1
Com-RuO ₂	1.20	---	106.5

Table S3. The overpotential at 10 mA cm⁻² and mass activity at 1.53 V of different catalysts.

Catalyst	Overpotential (mV)	Mass activity (A·g⁻¹)
FePb-RuO ₂	194	957.4
Fe-RuO ₂	196	202.1
Pb-RuO ₂	224	159.5
Hm-RuO ₂	257	73.5
Com-RuO ₂	311	13.5

Table S4. C_{dl} and ECSA of different catalysts.

Catalyst	C_{dl} (mF cm⁻²)	ECSA (cm²)
FePb-RuO ₂	63.85	1824.29
Fe-RuO ₂	45.89	1311.14
Pb-RuO ₂	28.37	810.57
Hm-RuO ₂	8.18	233.71
Com-RuO ₂	0.63	18

Table S5. ICP-OES results for the catalyst after OER.

Catalyst	Ru in electrolyte (mg)	Other elements in electrolyte (mg)
FePb-RuO ₂	0.021	Fe-0.002 Pb-0.003
Fe-RuO ₂	0.073	Fe-0.007
Pb-RuO ₂	0.057	Pb-0.006
Hm-RuO ₂	0.092	/
Com-RuO ₂	0.116	/

Table S6. The comparison of OER performance of the FePb-RuO₂ with recently reported electrocatalysts in acid media.

Catalyst	Electrolyte	η_{10} (mV)	Stability	$\Delta\eta_{10}$ (mV)	Ref.
FePb-RuO ₂	0.5 M H ₂ SO ₄	194	100 h	44	This work
Cu-RuO ₂	0.5 M H ₂ SO ₄	188	8 h	83	9
Co-RuO ₂	0.5 M H ₂ SO ₄	169	10000	15	10
RuNi NAs	0.5 M H ₂ SO ₄	252	10 h	/	11
E-Ru/Fe ONAs	0.5 M H ₂ SO ₄	238	9 h	/	12
Ru@RuO ₂	0.5 M H ₂ SO ₄	191	20 h	97	13
RuO ₂ NSs	0.5 M H ₂ SO ₄	199	6 h	32	14
Mn-RuO ₂	0.5 M H ₂ SO ₄	158	10 h	370	15
Cr _{0.6} Ru _{0.4} O ₂	0.5 M H ₂ SO ₄	178	10 h	/	16
RuPbO _x	0.5 M H ₂ SO ₄	191	100 h	85	17
RuO ₂ NWs	0.1 M HClO ₄	224	12 h	/	18
S-RuFeO _x	0.1 M HClO ₄	187	10 h	20	19
Pt-RuO ₂	0.5 M H ₂ SO ₄	228	100 h	/	20
Ni-Ru@RuO _x	0.5 M H ₂ SO ₄	184	30 h	/	21
a/c RuO ₂	0.1 M HClO ₄	205	60 h	/	22
Ru ₁ -Pt ₃ Cu	0.1 M HClO ₄	220	29 h	/	23

References

- [1] Kresse, G.; Furthmüller, J. Efficient Iterative Schemes for Ab Initio Total-Energy Calculations Using a Plane-Wave Basis Set. *Phys. Rev. B* **1996**, *54*, 11169–11186.
- [2] Kresse, G.; Furthmüller, J. Efficiency of Ab-Initio Total Energy Calculations for Metals and Semiconductors Using a Plane-Wave Basis Set. *Comp. Mater. Sci.* **1996**, *6*, 15–50.
- [3] Kresse, G.; Joubert, D. From Ultrasoft Pseudopotentials to the Projector Augmented-Wave Method. *Phys. Rev. B* **1999**, *59*, 1758–1775.
- [4] Blöchl, P. E. Projector Augmented-Wave Method. *Phys. Rev. B* **1994**, *50*, 17953–17979.
- [5] Perdew, J. P.; Burke, K.; Ernzerhof, M. Generalized Gradient Approximation Made Simple. *Phys. Rev. Lett.* **1996**, *77*, 3865–3868.
- [6] Monkhorst, H. J.; Pack, J. D. Special Points for Brillouin-Zone Integrations. *Phys. Rev. B* **1976**, *13*, 5188.
- [7] Jain, A.; Hautier, G.; Moore, C. J.; Ong, S. P.; Fischer, C. C.; Mueller, T.; Persson, K. A.; Ceder, G. A High-Throughput Infrastructure for Density Functional Theory Calculations. *Comp. Mater. Sci.* **2011**, *50*, 2295–2310.
- [8] Nørskov, J. K.; Rossmeisl, J.; Logadottir, A.; Lindqvist, L.; Kitchin, J. R.; Bligaard, T.; Jonsson, H. Origin of the Overpotential for Oxygen Reduction at a Fuel-Cell Cathode. *J. Phys. Chem. B* **2004**, *108*, 17886–17892.

- [9] Su, J.; Ge, R.; Jiang, K.; Dong, Y.; Hao, F.; Tian, Z.; Chen, G.; Chen, L. Assembling Ultrasmall Copper-Doped Ruthenium Oxide Nanocrystals into Hollow Porous Polyhedra: Highly Robust Electrocatalysts for Oxygen Evolution in Acidic Media. *Adv. Mater.* **2018**, *30*, 1801351.
- [10] Tian, Y.; Wang, S.; Velasco, E.; Yang, Y.; Cao, L.; Zhang, L.; Li, X.; Lin, Y.; Zhang, Q.; Chen, L. A Co-Doped Nanorod-Like RuO₂ Electrocatalyst with Abundant Oxygen Vacancies for Acidic Water Oxidation. *iScience* **2020**, *23*, 100756.
- [11] Yang, J.; Shao, Q.; Huang, B.; Sun, M.; Huang, X. pH-Universal Water Splitting Catalyst: Ru-Ni Nanosheet Assemblies. *iScience* **2019**, *11*, 492–504.
- [12] Yao, Q.; Huang, B.; Xu, Y.; Li, L.; Shao, Q.; Huang, X. A Chemical Etching Strategy to Improve and Stabilize RuO₂-Based Nanoassemblies for Acidic Oxygen Evolution. *Nano Energy* **2021**, *84*, 105909.
- [13] Wen, Y.; Yang, T.; Cheng, C.; Zhao, X.; Liu, E.; Yang, J. Engineering Ru(IV) Charge Density in Ru@RuO₂ Core-Shell Electrocatalyst Via Tensile Strain for Efficient Oxygen Evolution in Acidic Media. *Chin. J. Catal.* **2020**, *41*, 1161–1167.
- [14] Zhao, Z. L.; Wang, Q.; Huang, X.; Feng, Q.; Gu, S.; Zhang, Z.; Xu, H.; Zeng, L.; Gu, M.; Li, H. Boosting the Oxygen Evolution Reaction Using Defect-Rich Ultra-Thin Ruthenium Oxide Nanosheets in Acidic Media. *Energy Environ. Sci.* **2020**, *13*, 5143–5151.

- [15] Chen, S.; Huang, H.; Jiang, P.; Yang, K.; Diao, J.; Gong, S.; Liu, S.; Huang, M.; Wang, H.; Chen, Q. Mn-Doped RuO₂ Nanocrystals as Highly Active Electrocatalysts for Enhanced Oxygen Evolution in Acidic Media. *ACS Catal.* **2019**, *10*, 1152–1160.
- [16] Lin, Y.; Tian, Z.; Zhang, L.; Ma, J.; Jiang, Z.; Deibert, B. J.; Ge, R.; Chen, L. Chromium-Ruthenium Oxide Solid Solution Electrocatalyst for Highly Efficient Oxygen Evolution Reaction in Acidic Media. *Nat. Commun.* **2019**, *10*, 162.
- [17] Huang, R.; Wen, Y.; Peng, H.; Zhang, B. Improved Kinetics of OER on Ru-Pb Binary Electrocatalyst by Decoupling Proton-Electron Transfer. *Chin. J. Catal.* **2022**, *43*, 130–138.
- [18] Chen, L.; Li, Y.; Liang, X. Ar/H₂/O₂-Controlled Growth Thermodynamics and Kinetics to Create Zero-, One-, and Two-Dimensional Ruthenium Nanocrystals Towards Acidic Overall Water Splitting. *Adv. Funct. Mater.* **2021**, *31*, 2007344.
- [19] Xue, Y.; Fang, J.; Wang, X.; Xu, Z.; Zhang, Y.; Lv, Q.; Liu, M.; Zhu, W.; Zhuang, Z. Sulfate-Functionalized RuFeO_x as Highly Efficient Oxygen Evolution Reaction Electrocatalyst in Acid. *Adv. Funct. Mater.* **2021**, *31*, 2101405.
- [20] Wang, J.; Yang, H.; Li, F.; Li, L.; Wu, J.; Liu, S.; Cheng, T.; Xu, Y.; Shao, Q.; Huang, X. Single-Site Pt-Doped RuO₂ Hollow Nanospheres with Interstitial C for High-Performance Acidic Overall Water Splitting. *Sci. Adv.* **2022**, *8*, eabl9271.
- [21] Harzandi, A. M.; Shadman, S.; Nissimagoudar, A. S.; Kim, D. Y.; Lim, H. D.; Lee, J. H.; Kim, M. G.; Jeong, H. Y.; Kim, Y.; Kim, K. S. Ruthenium Core-Shell Engineering with Nickel

Single Atoms for Selective Oxygen Evolution Via Nondestructive Mechanism. *Adv. Energy Mater.* **2021**, *11*, 2003448.

[22] Zhang, L.; Jang, H.; Liu, H.; Kim, M. G.; Yang, D.; Liu, S.; Liu, X.; Cho, J. Sodium-Decorated Amorphous/Crystalline RuO₂ with Rich Oxygen Vacancies: A Robust pH-Universal Oxygen Evolution Electrocatalyst. *Angew. Chem., Int. Ed.* **2021**, *60*, 18821–18829.

[23] Yao, Y.; Hu, S.; Chen, W.; Huang, Z.-Q.; Wei, W.; Yao, T.; Liu, R.; Zang, K.; Wang, X.; Wu, G.; Yuan, W.; Yuan, T.; Zhu, B.; Liu, W.; Li, Z.; He, D.; Xue, Z.; Wang, Y.; Zheng, X.; Dong, J.; Chang, C.-R.; Chen, Y.; Hong, X.; Luo, J.; Wei, S.; Li, W.-X.; Strasser, P.; Wu, Y.; Li, Y. Engineering the Electronic Structure of Single Atom Ru Sites Via Compressive Strain Boosts Acidic Water Oxidation Electrocatalysis. *Nat. Catal.* **2019**, *2*, 304–313.